

See discussions, stats, and author profiles for this publication at: <https://www.researchgate.net/publication/327898895>

Robotic Arm Based Automatic Ultrasound Scanning for Three-Dimensional Imaging

Article in IEEE Transactions on Industrial Informatics · September 2018

DOI: 10.1109/TII.2018.2871864

CITATIONS

81

READS

660

3 authors, including:



Qinghua Huang

Northwestern Polytechnical University

151 PUBLICATIONS 2,996 CITATIONS

SEE PROFILE

Robotic Arm Based Automatic Ultrasound Scanning for Three-Dimensional Imaging

Abstract—This paper presents a human skin inspired automatic robotic ultrasound (US) system for three dimensional (3D) imaging. A depth camera was adopted to capture the point cloud of the skin surface. According to 3D contour of the skin surface, the scan range and scan path for the US probe could be automatically determined. Then we used a normal vector-based method to determine the pose of the robotic arm corresponding to each scan point in the scan path. In addition, two force sensors could feedback the contact force between the scanned tissue and the emission plane of the probe for fine-tuning the pose of the robotic arm. After the scanning, the system could realize 3D ultrasound reconstruction. Experimental results validate the feasibility of the proposed system. It is expected that the proposed system will be useful in clinical practices.

Index Terms—Automatic scanning; Robotic 3D ultrasound; Robotic arm; Scan path planning.

I. INTRODUCTION

As an indispensable diagnosis-aid technology, ultrasound (US) examination is of increasing importance in recent years [1]. It could provide the B-scan with low cost and no radiation in real time [2]. The use of US would even increase in daily medicine and healthcare routines in the future. Traditional two dimensional (2D) US can dynamically display 2D images of the region of interest (ROI) [3]. However, the lack of 3D anatomy information makes the diagnosis result heavily depend on the subjective experience of the doctor. The 3D US can overcome this serious limitation [4]-[9]. 3D US imaging can be conducted with three main steps: Firstly, collect the raw B-scans labeled with corresponding spatial information; secondly, reconstruct the 3D volume; and finally, render and display the 3D volume. Every step has a significant influence on the accuracy of 3D imaging. Except for systems using 2D arrays, 3D US images are reconstructed from raw B-scans, with their respective spatial information. Therefore, the scanning manners (especially the skills for manipulating the probe) and precise recording of position and orientation of B-scans were very important to ensure correct 3D reconstruction. Only based on accurate 3D ultrasound imaging data, 3D image analysis [10] [11] can be further realized.

However, the probe in a conventional freehand 3D US system is held by operator during the scanning. This often leads to the jitter of the probe, hence bringing positional errors into

the subsequent volume reconstruction. To overcome this drawback, researchers developed mechanical scanning devices to precisely regulate the probe motion. Nevertheless, those devices drive the probe to move in a strictly predefined path (e.g. linear or rotational movement), making the scanning less flexible. Thus, we consider using a robot arm to act as a human's hand during the probe scanning

Medical robotics have been used in many fields including rehabilitation [12]-[14], minimally invasive surgery [15]-[17], and image-guided interventions [18] and so on. Robotic ultrasound systems (RUS) combined the US examination with the robotic system in medical interventions [19]. The obvious advantages that the robot system possess, i.e. stability, high accuracy, repeatability, dexterity, maneuverability, can improve the performance of US system in terms of acquisition and manipulation. For 3D US imaging, with the robot actuating the probe to scan, the system could precisely track and locate the B-scans, which can improve the accuracy of volume construction. Moreover, these robots do not suffer from human afflictions such as hand-tremor, fatigue, etc.

In the past two decades, benefiting from the major advances in robot technology, more and more investigators and commercial companies have developed their RUS. The da Vinci Surgical System which may be the most well-known medical assistant, [20], consisted of a surgeon console, a patient-side cart, endwrist instruments, and a vision system. The system would augment operator's ability to achieve high precision, safety, stability, and minimally invasive surgery. ACUSON S2000TM ABVS[21] (Automated Breast Volume Scanner, Siemens AG, Germany), a worldwide clinical examination apparatus, could automatically scan the patient's breast in the supine position to acquire full-field volume. Huang *et al.*[22] developed a linear tracking system for 3D medical US imaging, in which one degree of freedom linear

track combined the advantages of both mechanical scanning and freehand scanning. The same group [23] used the same linear tracking system for realizing quasi-static 3D US elastography. Chen *et al* [24] used a 3D translating device to hold the US probe, and mechanically scan the tissues in a predefined manner. The operator could set the compress depth and step length. The constant compression pressure and semi-automatic scanning could generate high-quality 3D strain images and present incremental volume reconstruction and volume rendering in near real-time. However, there is little flexibility because the probe could only be moved along a single line. Janvier *et al*. [25] used the F3 Articulated Robot to acquire 2D US images for subsequent 3D-reconstruction. For each scanned leg, the operator manually moves the robotic arm in teach mode. In replay mode, the robotic arm would replay the taught path to acquire 2D images. However, the patient leg may move when switching the teach mode to the replay mode. In recent years, the same group [26] developed an automatic vessel tracking strategy as the alternative of teach mode and replay mode. The whole system was applied to provide the 3D results of lower limb arteries. The system would calculate the distance between the center of the vessel and the center element of the probe, and the F3 Articulated Robot would correct the trajectory to maintain the artery at the center of the B-scan. Then the F3 Articulated Robot could step along its z-axis to complete its trajectory. However, the system performance would heavily depend on the detection and tracking of the vessels. Conti [27] developed a collaborative robotic system to assist scanning. The operator would control the slave robot in tele-operation mode or semi-automatic mode. A force controller would maintain the constant contact between the probe and tissue surface. The 3D reconstructed view would be computed in real time. The focus of the whole system was to reduce doctors' fatigue caused by heavy working load. Meng [28] developed a novel robotic US scanning system to scan the lower limbs. The operator manipulates one robot arm to inspect one leg. Another robot arm would mimic the mirrored motion to scan another leg based on the point cloud obtained by the RGB-D camera. However, its application was limited to scan the leg and there was lack of force information.

In this study, we proposed a 6-DoF robotic US system for three dimensional (3D) imaging. The Kinect was adopted to acquire the contour of the tissue surface. With respect to an experience based rule, the system would determine the point cloud of the scan range. Two scan-path planning modes were designed to extract the scan points from the point cloud. Based on these scan points, we designed a normal-vector based method to determine the pose of robotic arm and actuate the center point of probe to touch the desired point. In addition, two force sensors attached to the left and right sides of the front face of the probe, respectively, were used to feedback the contact force for fine-tuning the robot pose and guarantying the safety. Having completed the scanning progress, the system would collect the B-scans labeled with corresponding spatial information for subsequent volume construction. The paper is organized as follows. Section II describes the system architecture, system calibration, and the working procedures.

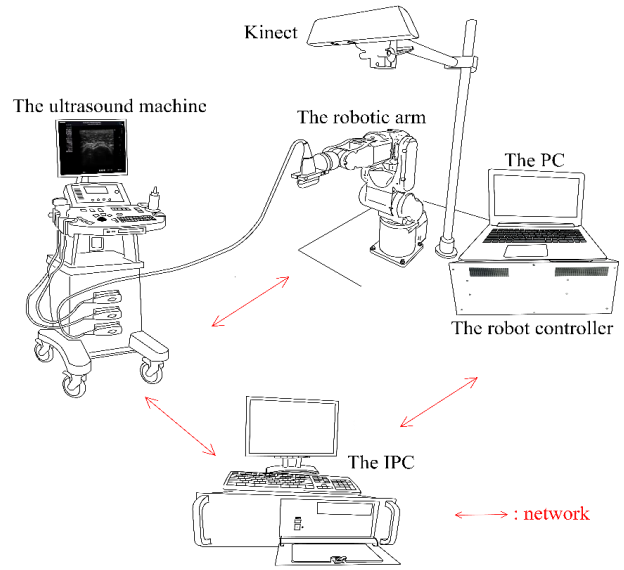


Fig. 1. Illustration of the proposed system.

Section III reports the experimental results of US phantoms and a human forearm. Section IV gives a discussion of the proposed system and draws conclusions finally.

II. METHODS

A. System Design

The proposed system consisted of the following parts: an US machine (Sonix RP, Ultrasonic Medical Corporation, Canada) with a linear array probe (L9-4/38) for acquiring the B-scans, a 6-DoF robotic arm (Epson C4-A601S, Seiko Epson Corporation, Japan) for actuating the probe, a personal computer (PC) with an Intel Core i5-3317U and 6 GB RAM for controlling the robotic arm, a depth camera (Kinect, Microsoft Corporation, USA) for obtaining the 3D contour of the tissue, and an industry personal computer (IPC, EVOC Intelligent Technology Co., Ltd., China) for collecting the B-scans and their positional information for the subsequent volume reconstruction. Two force sensors (RFP-601, yubo Inc., China) connecting to a data acquisition card (DAQ card, NI USB-6000, National Instruments Corporation, USA) feedbacked the contact force between the probe emission plane and tissue surfaces for fine-tuning the robotic arm. The server, US machine, and the IPC were directly connected to a network (100Mbps), and the protocol of data transmission was TCP/IP.

The depth camera plays the role of perceiving the outside in our system as in the simultaneous localization and mapping (SLAM) system [29]. As illustrated in Fig. 1, the Kinect was attached to the end of the customized steel bracket, which was 30cm higher than the robotic arm. Both the depth image and the color image have a resolution of 640×480. Before acquiring the point cloud in the Kinect coordinate system K , the system registered the depth image and the color image as reported in [30]. The pixels in the color image could be transformed to K as follows:



Fig. 2. Illustration of the robot base coordinate system \mathbf{R} and the gripper coordinate system \mathbf{G} .

$$\begin{aligned} x_k &= (x_d - 320) \times z_d \times \frac{1}{f} \\ y_k &= (y_d - 240) \times z_d \times \frac{1}{f} \\ z_k &= z_d \end{aligned} \quad (1)$$

where (x_d, y_d) is the coordinate of the d th pixel in the color image, z_d is the depth of the pixel in the depth image, f is the focal length (i.e. 525 pixels) of the infrared camera in the Kinect. (x_k, y_k, z_k) is the coordinate of the pixel with respect to \mathbf{K} . The center point (320,240) is defined as the origin of the color image.

As illustrated in Fig. 2, two coordinate systems: i.e. the robot base coordinate system \mathbf{R} and the gripper coordinate system \mathbf{G} are associated with the 6-DOF robotic arm. To fix the probe, we installed a stainless steel clip on the flange of the 6th arm. The probe emits US waves and receives US echoes and the US machine generates the B-scan images according to the echoes received by the probe. Therefore, there should be a coordinate system of the B-scan image plane (denoted as \mathbf{B}) under the probe.

The robotic arm was equipped with a software development kits (EPSON RC+ 7.0) for developing the application software. EPSON RC+ 7.0 was connected to the robot controller, and the TEACH operation mode of [Robot Manager] in EPSON RC+ 7.0 offers a functional panel for changing the six DoF. The operator could use this mode to control the movement of robotic arm manually. Based on a dynamic link library (SpelNetLib70.dll), a custom-designed software system developed using the mixed programming of C# and C++ in Visual Studio 2010 (Microsoft Corporation, USA) could read the configurations of the robotic arm in real time. The configurations include the pose of the robotic arm (i.e. the

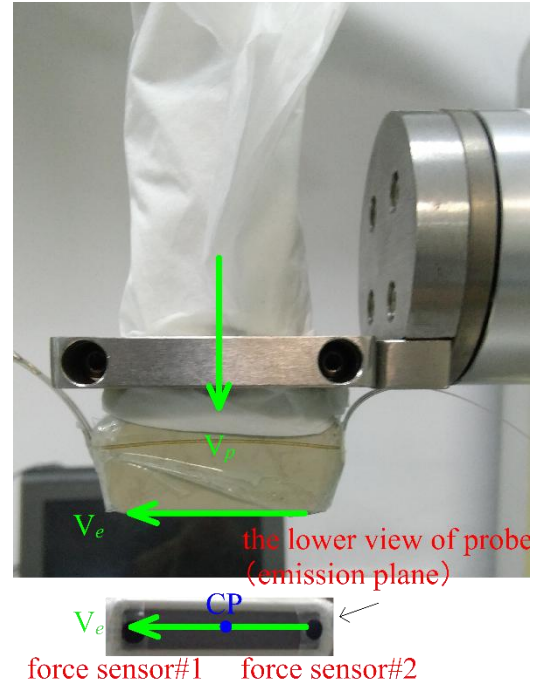


Fig. 3. Illustration of the probe with the two force sensors. V_p represents the unit vector which was perpendicular to the emission plane of the probe; and V_e represents the unit vector which was parallel to the midline of the emission plane of the probe. These two vectors could determine the pose of the probe.

position of the gripper with respect to \mathbf{R}), the moving speed, the moving acceleration, and the rotation mode. Among these configurations, the most useful information should be the pose of the robotic arm:

$${}^{gripper}\mathbf{P}_R = (X, Y, Z, U, V, W) \quad (2)$$

where ${}^{gripper}\mathbf{P}_R$ has six DoF: i.e. three translations (X, Y, Z) and three rotations (U, V, W) . The order of rotations was as the following: rotate first about x axis of \mathbf{R} by angle W , then about y axis of \mathbf{R} by angle V , and finally, about z axis of \mathbf{R} by angle U .

As illustrated in Fig. 3, two force sensors were attached to the left and right sides of the front face of the probe. The force sensors were slim and soft. The effective range of the force measurement was the black area with a diameter of 7mm. Although the force sensors produced a small shadow on the marginal sides of the B-scan image, the imaging performance was not apparently alleviated. The max value of force measurement was 9.8N (1kg). The force sensor outputs the measured force as the voltage signal that is negatively correlated with the force and could be read and digitized by the DAQ card.

B. System Calibration

Calibration (including spatial calibration and temporal calibration) is a key requirement of the conventional 3D US system. Normally, the spatial calibration aims to find the spatial relationship between the B-scan image plane and the positional sensor. In this study, we needed an additional spatial calibration to find the transformation between \mathbf{K} and \mathbf{R} because the automatic operation of the US scanning was inspired by the 3D

contours of the human skin surface which was captured by the Kinect instead of human eyes. In conventional 3D US imaging, the temporal calibration is used to find the time offset between the B-scan images and their positional labels. In our system, the IPC could directly read the pose of the robotic arm in real-time, and the robotic arm would move to the next scan point only after successful collection of the current B-scan in current point. It is therefore no need to find the time offset between the positional data and the B-scans. As a result, the proposed system requires only the two sorts of spatial calibration.

To produce a 3D US image, the pixels from the raw B-scans should be projected onto the voxel grids in a predefined volume data set. Then a reconstruction algorithm is used to interpolate and adjust the intensity value of each voxel. Consequently, each pixel in the B-scan coordinate system B should be firstly transformed to the gripper coordinate system G , then to the robot base coordinate system R , and finally to the volume coordinate system C . The coordinate transformation is described as below:

$$P_C = {}^C T_R {}^R T_G {}^G T_B P_B \quad (3)$$

where

$$P_B = \begin{pmatrix} s_x u \\ s_y v \\ 0 \\ 1 \end{pmatrix} \quad (4)$$

In the above equation, (u, v) denotes the position of a pixel in B , s_x and s_y denote the scale factors in x - and y -axes, respectively, thus P_B represents a 3D vector corresponding to the pixel, and P_C represents the corresponding vector of the pixel (u, v) in the volume coordinates. Please note that the form of ${}^T T_S$ represents the transformation matrix from coordinate system S to coordinate system T . As mentioned before, ${}^R T_G$ could be read directly from the pose of the robotic arm (X, Y, Z, U, V, W) . ${}^C T_R$ could be determined by the reconstruction methods. That leaves the ${}^G T_B$ unknown only, which could be estimated using a cross-wire method [31]. During the scanning, the robotic arm should actuate the probe to let the center position (CP) of probe emission plane match the coordinate values of the surface in R . Since the center position (CP) of probe was not considered in G . After estimating the ${}^G T_B$, this vector ${}^{CP} V_G$ (the CP with respect to G) would be obtained by calculating the coordinate value of the center pixel of the first row (i.e. (1,320)) in G .

The second spatial calibration aimed to estimate ${}^R T_K$ (i.e. the spatial relationship between K and R). This calibration could be executed by obtaining two coordinate system expressions of the same point in world coordinate system. The

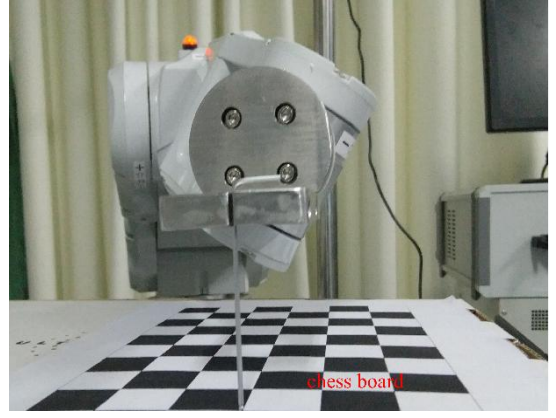


Fig. 4. Illustration of the tip calibration. The robotic arm would actuate the steel needle to touch the cross intersection one by one.

second spatial calibration made use of a chessboard paper with 6×10 rectangles each of which is of $1.75\text{cm} \times 1.75\text{cm}$. We fixed a steel needle using a clip attached to the gripper. The operator manually recorded the 3D coordinate values in K of 45 cross intersections on the chessboard, then controlled the robotic arm in TEACH operation mode to actuate the probe to let the tip coincide with the intersection points one by one as illustrated in Fig. 4. Defining (x_K, y_K, z_K) as the 3D coordinate values of the cross intersections in K , and $(x_G, y_G, z_G, u_G, v_G, w_G)$ as the pose of the robotic arm corresponding to each intersections. As illustrated in Fig. 2, a tip with respect to R could be determined by [33]:

$${}^T V_R = {}^{gripper} V_R + {}^R E_G \times {}^T V_G \quad (5)$$

where ${}^T V_G$ represents the unknown vector of the tip in the gripper coordinate system G , ${}^{gripper} V_R$ represents the known position vector of the gripper in R , i.e. $(x_G, y_G, z_G)^T$, ${}^R E_G$ represents the known Euler rotation matrices (three parameters were (u_G, v_G, w_G)) that transform the gripper orientation in R , and ${}^T V_R$ represents the vector of the tip in R . ${}^T V_G$ could be estimated by controlling the robotic arm to actuate the steel needle to make the tip touch one pointed end in different robot poses. Once the ${}^T V_G$ (the tip vector with respect to G) was estimated, the position of the tip (x_R, y_R, z_R) with respect to R could be calculated using (5). In our actual experiment, the error was very large and the results cannot converge. The units of the K and R were mm, while the 1mm in K was not the same as 1mm in R actually. The ratio of the three axes (r_x, r_y, r_z) should be added, therefore, the nonlinear homogeneous equations would be:

$$\begin{pmatrix} x_R \\ y_R \\ z_R \\ 1 \end{pmatrix} = {}^R T_K \begin{pmatrix} r_x x_K \\ r_y y_K \\ r_z z_K \\ 1 \end{pmatrix} \quad (6)$$

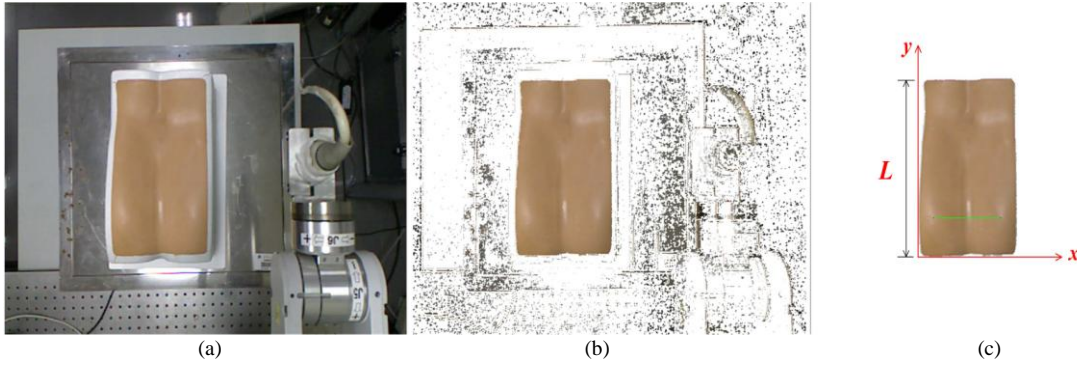


Fig. 5. Scan range extraction of the lumbar phantom. (a) Original color image of the Kinect. (b) Segmented contours. The pixels unsatisfying the Red>Green>Blue rules were set to be white. (c) The range of the scanned tissue. The green line represents the scan path.

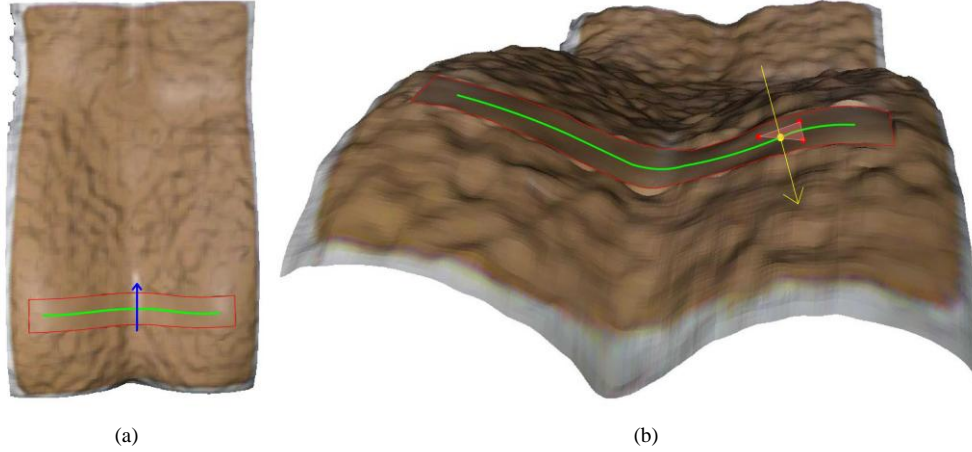


Fig. 6. Illustration of the normal vector-based method. (a) The 3D contour of the processed lumbar phantom. (b) The normal vector-based method in lumbar phantom. The green line represents the scan path, the blue vector represents the normal vector of scan path in the X-Y plane of the R , and the red block represents the smooth area. Three red point around the yellow point could form a triangle to be calculated the normal vector (yellow vector) as the normal vector of the plane where the yellow point lay.

C. Scan path

Once the proposed system was calibrated, the system could transform the scan points in the point cloud of the tissue surface from K to R . First of all, we extracted the scan range using an experience based rule (i.e. the points in the area of interest take the property of Red>Green>Blue) [30] and then determined the scan points. Fig.5 shows the scan range extraction of the lumbar phantom. The proposed system was applicable to the single sweep. Let the vertical direction of the color image be the y direction, the direction perpendicular to y be the x direction, and the probe's width be w . If the length of the scan range (L) in the y direction was smaller than $2w$, the midline of the scan range ($0.5L$) in the x direction was set to be the scan path. Otherwise, the system would extract the scan path in the x direction. To avoid the transition region of the edge, this scan path would be shortened in two sides. Otherwise, the system would determine the line in $\alpha L(w/L < \alpha < (L-w)/L)$ of y direction as the scan path. α is a parameter and could be set by default or adjusted by the user. Except this automatic approach to setting the scan path, we offer an alternative way to extract the scan path, i.e. the user could draw a straight line on the color image of the Kinect. The pixels in this line were treated as the scan path.

D. Pose of the robotic arm

Having extracted the point cloud of scan path in K , the system could use the transformation relationship to translate these points to R . The robot arm should actuate the probe to let the CP of probe coincide with the scan point along the scan path in R . There are a lot of poses of the robotic arm to fix the CP of probe in the same point. To obtain the B-scans with good quality, the six parameters of the gripper (X, Y, Z, U, V, W) corresponding to each scan point should be carefully determined.

In manually US scanning, the operator often holds and adjusts the pose of the probe on the tissue surface to achieve the best US image. Normally, the probe should be approximately perpendicular to the tissue surface and have a close contact with the skin. Thus, we developed a normal vector-based method to determine the six parameters of gripper. As illustrated in Fig.3, the probe can be represented by two unit vectors, i.e. V_p and V_e . V_p in the initial state was $(0, 0, -1)$ with respect to R , and $(-1, 0, 0)$ with respect to G . V_e in the initial state was $(0, 1, 0)$ with respect to R , and $(0, 0, 1)$ with respect to G . To improve efficiency without losing accuracy, we extracted the point cloud of the plane around the scan path to carry on the whole smoothness. Fig.6 (a) shows the processed 3D contour of

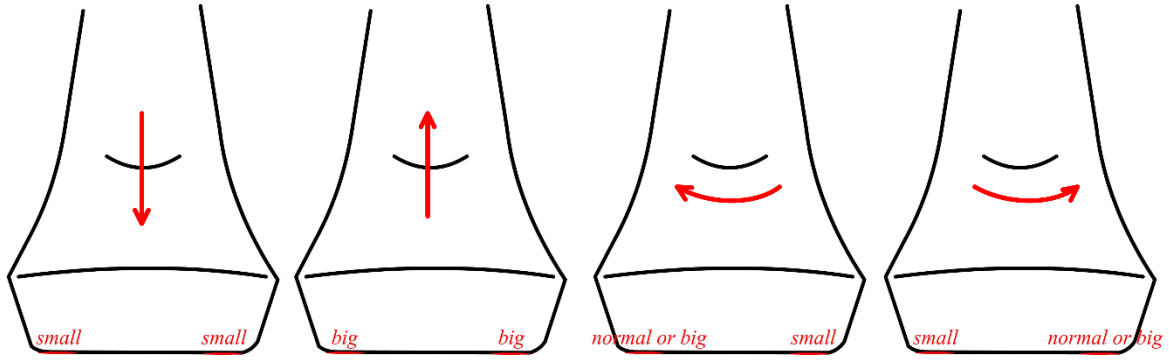


Fig. 7. Illustration of the probe adjustment according to the feedback signals from the two force sensors. The red vector represents the direction of the adjustment. The first two directions are parallel to the V_p , and the rotation axis of the next two rotations is the same vector which is perpendicular to V_p and V_e .

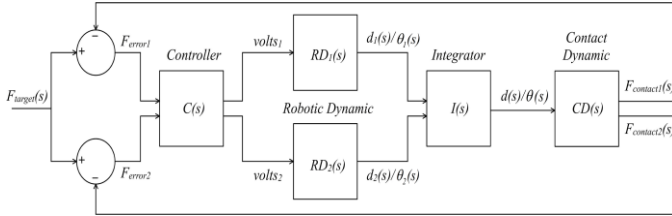


Fig. 8. Block diagram of the closed-loop force control system.

lumbar phantom. Given a scan point in the scan path, the system could automatically adjust the pose of the probe to make V_p parallel to the normal vector of the tissue surface where the scan point lay.

As shown in Fig.6, the green dot line represents the scan path, and the blue point represents one scan point in the green scan path. The blue vector represents the normal vector of the scan path in the X-Y plane of the R . The system would let the V_e parallel with the blue vector in the first place. Three red points around the yellow point formed a triangle to represent the plane where the yellow point lay. The system could calculate the normal vector (i.e. the yellow vector) of the yellow point. The normal vector of each scan point would be obtained in the same way. Once the V_p was determined, the (U, V, W) of the robotic arm would be calculated by quaternion conversion and Euler conversion [35]. Then (X, Y, Z) of the robotic arm could be determined by (5). The pose of the robotic arm corresponding to each scan point could therefore be determined.

E. Probe scanning method

Due to the limited accuracy of point cloud and some inevitable errors, e.g. small tissue moving and light interference, the scan path could not always perfectly match the tissue surface. The contact force between the probe emission plane and the scanned tissue could reflect the matching degree. According to the two force values during the scanning, the system would adjust the pose of robotic arm to make the two force values fall in [1N, 8N] generally. This force range was determined with reference to previous studies [36]-[38] and our preliminary tests. The target force F_{target} and the floating size f could be set by the operator. Both the force values should fall

into a normal range ($F_{target} - f < F_{contact} < F_{target} + f$). If both the values were smaller than $F_{target} - f$, the robotic arm would make the probe closer to the tissue by d along V_p (the same as the normal vector of the scan point). If the values of the two force sensor were both greater than $F_{target} + f$, the robotic arm would move the probe far away from the tissue surface by d along V_p . If one force value was smaller than $F_{target} - f$ and the other was normal or greater, the robotic arm would rotate about the normal vector of the probe plane by an angle θ in the opposite direction of the smaller force. Fig. 7 shows the illustration of the probe adjustment according to two force sensor readings. The adjustment would be suspended until two values fell into the normal range. Fig. 8 gives the block diagram of the closed-loop force control system. The controller $C(s)$ would transform the error between the target force and contact force to a voltage. This voltage could result in an adjustment of d/θ . Then the integrator $I(s)$ could integrate d_1/θ_1 and d_2/θ_2 to obtain d/θ . The max value of d was 0.2 mm, and that θ of was 0.2 degree.

F. Working procedures

The workflow of the proposed system is summarized as follows:

- (1) Boot and reset the robot arm in low power mode. Start the ultrasound machine for collecting the B-scans.
- (2) Connect the IPC, PC, and the ultrasound machine through the local area network.
- (3) The system uses the Kinect to acquire the point cloud of the scanned tissue and extracts the scan path. For each scan point, the desired pose of robotic arm can be calculated.
- (4) The robotic arm would rotate first to let V_e be parallel to the normal vector of the scan path in the X-Y plane of the R .
- (5) The robotic arm holds the probe to the scan point with corresponding pose. If two force values were not in the normal range, the system would adjust the pose slightly according to abovementioned rules until two force values fall into the normal range.
- (6) The PC sends a signal to the ultrasound machine to inform that this scan point was done. Then the ultrasound

machine sends the buffer of B-scan to the IPC. Meanwhile, the PC sends the current pose of the robotic arm to the IPC. For each scan point, the IPC records one B-scan and one pose of the

TABLE I. EXPERIMENTAL PARAMETERS

| Parameter | Values |
|---|--|
| ${}^T V_G$ (the tip vector in G) | $(79.56 \pm 0.1 \text{mm}, -3.19 \pm 0.09 \text{mm}, 79.24 \pm 0.09 \text{mm})$ |
| ${}^{CP} V_G$ (the CP vector in G) | $(-58.19 \pm 0.15 \text{mm}, -2.23 \pm 0.28 \text{mm}, 47.78 \pm 0.11 \text{mm})$ |
| $s_x, s_y, {}^G T_p(x, y, z, \alpha, \beta, \gamma)$ (first spatial calibration) | $0.0121 \pm 0.00 \text{mm/pixel}, 0.0113 \pm 0.00 \text{mm/pixel},$ $(-7.8196 \pm 0.12 \text{cm}, -0.4207 \pm 0.09 \text{cm}, 4.6417 \pm 0.03 \text{cm},$ $-1.5030 \pm 0.02 \text{rad}, -1.5074 \pm 0.04 \text{rad}, -3.0899 \pm 0.07 \text{rad})$ |
| $r_x, r_y, r_z, {}^R T_K(x, y, z, \alpha, \beta, \gamma)$ (second spatial calibration) | $0.9896, 1.0015, -0.9929$ $(-115.31 \pm 0.02 \text{mm}, 437.11 \pm 0.1 \text{mm}, -901.94 \pm 0.31 \text{mm},$ $0.0113 \pm 0.23 \text{rad}, 0.00 \pm 0.00 \text{rad}, -0.0678 \pm 0.02 \text{rad})$ |

TABLE II. SETTINGS AND PARAMETERS FOR *in vitro* AND *in vivo* EXPERIMENTS.

| Experiment | Frames | Scan time (s.) | Voxels (W×H×L) | Reconstruction time (s.) |
|------------|--------|-------------------|-------------------|-----------------------------|
| Thyroid | 102 | 82 | 96×106×262 | 8.7 |
| Breast | 71 | 56 | 96×106×141 | 5.3 |
| Lumbar | 115 | 81 | 96×106×318 | 9.7 |
| Forearm | 159 | 115 | 96×106×518 | 14.3 |



(a)

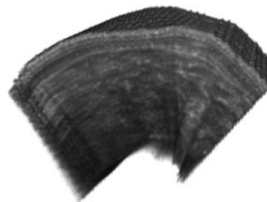


(b)

Fig. 9. Experimental results of scanning the thyroid phantom. (a) The picture of scanning the thyroid phantom. (b) The reconstruction thyroid volume.



(a)



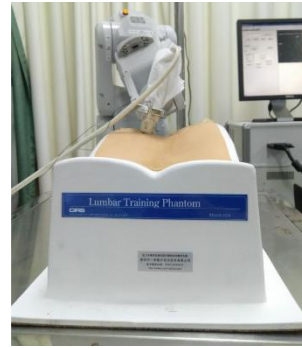
(b)

Fig. 10. Experimental results of scanning the breast phantom. (a) The picture of scanning the breast phantom. (b) The reconstruction breast volume.

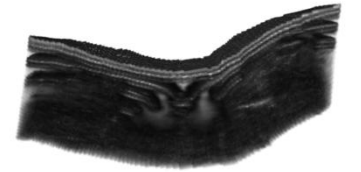
robotic arm for subsequent reconstruction.

(7) Repeat (5)-(6) until the scan path is completely traversed.

(8) After the automatic scanning, the system can perform the



(a)



(b)

Fig. 11. Experimental results of scanning the lumbar phantom. (a) The picture of scanning the lumbar phantom. (b) The reconstruction lumbar volume.

volume reconstruction and show the rendering results.

To well balance the efficiency and accuracy, the volume reconstruction was conducted using the Bezier interpolation method [39]. In this study, a 3rd order Bezier curve function determined by four control points was used to obtain the interpolated value of the voxels. For more technical details, please refer to [39].

III. EXPERIMENTAL RESULTS

The array length of the linear probe was 38 mm, its imaging depth was set to be 40 mm (adjustable), and the B-scan's resolution was 488×356. The calibration results were shown as Table I.

To test the performance of the proposed system in different tissues, we used it to scan a thyroid phantom, a breast phantom,

a lumbar phantom and real human forearm (the subject was male and 24 years old). Table II gives the experimental

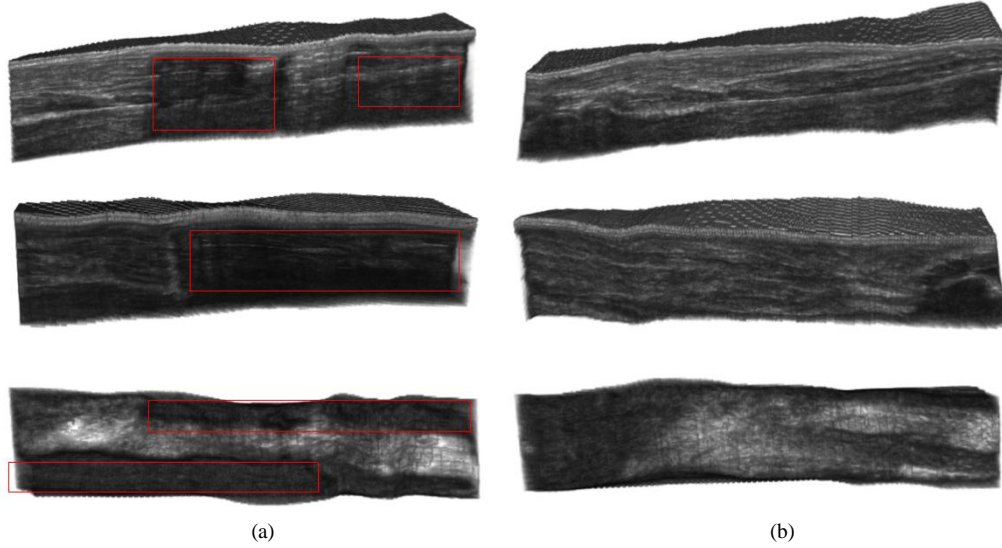


Fig. 12. Experimental results of scanning the forearm. (a) The reconstruction lumbar volume without force feedback (148 frames) in front view, back view, lower view. (b) The reconstruction lumbar volume with force feedback (159 frames) in front view, back view, lower view. The area in the red rectangle has block of empty voxels.

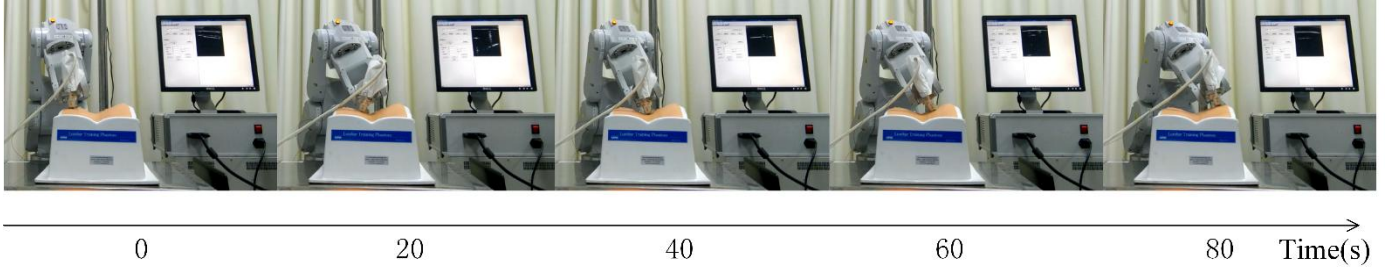


Fig. 13. Timeline of the scanning on the lumbar phantom.

parameters corresponding to these scanned object. Figs. 9-12 give the experimental results of the thyroid phantom (Model 074, CIRS, Inc., USA), breast phantom (Model 073, CIRS, Inc., USA), lumbar phantom (Model 034, CIRS, Inc., USA) and human forearm. From the figures, the thyroid, breast, lumbar, and the subject's forearm can be clearly observed, indicating that the proposed system has the advantages of high computing efficiency and good imaging quality. Note that Fig. 13 demonstrates the timeline of the scanning on the lumbar phantom and delineates the scanning process.

We also conducted the experiments of scanning forearm to compare the 3D US images with and without the feedback from the two force sensors. We found that the areas in the red rectangles in Fig. 13(a) were nearly empty. It can be envisaged that the probe might be slanting on the other side, i.e. the probe was not very well fitted to the skin surface. Without the force feedback, the probe could just scan the forearm rigidly. While in the scanning with the force feedback, the robotic arm could automatically adjust its pose to make the probe better fit the skin surface and to obtain better imaging results.

IV. DISCUSSION AND CONCLUSIONS

In this paper, we developed a novel robotic US system to perform automatic US scanning for 3D imaging. A 6-DoF robotic arm was used to actuate the probe to translate and rotate during the scanning. To achieve fully automatic scanning, we adopted the Kinect to acquire the point cloud of the scanned tissue, then automatically determined the scan range and scan path with respect to the 3D contour of skin surface, and transformed the scan path to the robot base coordinate system. According to the scan path, we designed a normal vector-based method to obtain the best pose of robotic arm for actuating the probe to contact the scan points in the scan path one by one. In addition, two force sensors attached to both front ends of probe emission plane could measure the contact force between the emission plane and the scanned tissue. The robotic arm could fine-tune its pose to produce good imaging quality and guarantee the safety. The main advantage of the proposed system is the fully automatic manipulation of the probe with adequate flexibility to achieve desired B-scan images. The system was not limited to scan a certain body part, but can be applied to various parts of human body. Experimental results

obtained from different phantoms and the human forearm have validated the feasibility of the proposed system.

However, this proposed system can work well in the case that the scanned body part should not have a wide range of movement. Otherwise, the scan range and the scan path should be incorrect and the system cannot adjust the scanning motion simultaneously. To overcome this problem, we will develop new functions using additional cameras or sensors in our future studies to monitor the movement of the body part during the scanning process and re-plan the scan path if necessary.

Although the proposed system cannot deal with moving body parts currently, it is expected to have good merit of clinical use because the patients are normally required to keep their body parts unmoved during a medical examination in a few minutes and most of them can make it well. In this case, our system can properly work and produce 3D US images with good quality. In conclusion, therefore, we expect that the proposed system can partially play the role of the US radiologists and act as a medical assistant to alleviate their work burden.

REFERENCES

- [1] Q. Huang, and Z. Zeng, "A Review on Real-Time 3D Ultrasound Imaging Technology," *Biomed Res Int.*, vol. 2017, no. 1, pp. 6027029, 2017.
- [2] S. W. Smith, G. E. Trahey, and O. T. von Ramm, "Two-dimensional arrays for medical ultrasound," *Ultrason. Imaging.*, vol. 14, no. 3, pp. 625–628, 1992.
- [3] T. Wang, J. Wu, and Q. Huang, "Enhanced Extended-Field-of-View ultrasound for musculoskeletal tissues using parallel computing," *Curr. Med. Imaging Rev.*, vol. 10, no. 4, pp. 237–245, 2014.
- [4] O. V. Solberg *et al.*, "Freehand 3D ultrasound reconstruction algorithms—a review," *Ultrasound Med. Biol.*, vol. 33, no. 7, pp. 991–1009, 2007.
- [5] Q. Huang and Y. Zheng, "Volume reconstruction of freehand three-dimensional ultrasound using median filters," *Ultrasonics*, vol. 48, no. 3, pp. 182–192, 2008.
- [6] Q. Huang *et al.*, "A new adaptive interpolation algorithm for 3D ultrasound imaging with speckle reduction and edge preservation," *Comput. Med. Imaging Graph.*, vol. 33, no. 2, pp. 100–110, 2009.
- [7] Q. Huang *et al.*, "Speckle suppression and contrast enhancement in reconstruction of freehand 3D ultrasound images using an adaptive distance-weighted method," *Appl. Acoust.*, vol. 70, no. 1, pp. 21–30, 2009.
- [8] D. Miller *et al.*, "Comparison of different reconstruction algorithms for three dimensional ultrasound imaging in a neurosurgical setting," *Int. J. Med. Robot. Comput. Assist. Surgery.*, vol. 8, pp. 348–359, 2012.
- [9] Z. Chen and Q. Huang, "Real-time freehand 3D ultrasound imaging," *Comput. Methods. Biomech. Biomed. Eng. Imaging. Vis.*, pp. 1–10, 2016.
- [10] S. Emmanouil *et al.*, "ATD: A Multiplatform for Semiautomatic 3-D Detection of Kidneys and Their Pathology in Real Time," *IEEE Trans. Human-Machine Syst.*, vol. 44, no. 1, pp. 146–153, 2014.
- [11] H. Chang *et al.*, "Graph-based learning for segmentation of 3D ultrasound images," *Neurocomputing*, vol. 151, no. 151, pp. 632–644, 2015.
- [12] D. Gan *et al.*, "Development of a exoskeleton robot for lower limb rehabilitation," *International Conference on Advanced Robotics and Mechatronics*, pp. 312–317, 2016.
- [13] Z. Li *et al.*, "Human-Robot Coordination Control of Robotic Exoskeletons by Skill Transfers," *IEEE Trans. Ind. Electron.*, vol. 64, no. 6, pp. 5171–5181, 2017.
- [14] Z. Li *et al.*, "Adaptive Impedance Control for an Upper Limb Robotic Exoskeleton Using Biological Signals," *IEEE Trans. Ind. Electron.*, vol. 64, no. 2, pp. 1664–1674, 2017.
- [15] A. Trejos *et al.*, "MIRA V: An integrated system for minimally invasive robot-assisted lung brachytherapy," *IEEE International Conference on Robotics and Automation*, pp. 1050–4729, 2008.
- [16] K. Zinchenko, C. Wu, and K. Song, "A Study on Speech Recognition Control for a Surgical Robot," *IEEE Trans. Ind. Informat.*, vol. 13, no. 2, pp. 607–615, 2017.
- [17] K. Lau *et al.*, "A Flexible Surgical Robotic System for Removal of Early-Stage Gastrointestinal Cancers by Endoscopic Submucosal Dissection," *IEEE Trans. Ind. Informat.*, vol. 12, no. 6, pp. 2365–2374, 2016.
- [18] G. Li *et al.*, "Robotic System for MRI-Guided Stereotactic Neurosurgery," *IEEE Rev. Biomed. Eng.*, vol. 62, no. 4, pp. 1077–1088, 2014.
- [19] A. M. Priester, S. Natarajan, and M. O. Culjat, "Robotic ultrasound systems in medicine," *IEEE Trans. Ultrason., Ferroelectr. Freq. Control*, vol. 60, no. 3, pp. 507–523, 2013.
- [20] Intuitive Surgical, [Online]. Available: https://www.intuitivesurgical.com/products/davinci_surgical_system/, accessed Jan 30, 2018.
- [21] SIEMENS Healthineers, [Online]. Available: <https://www.healthcare.siemens.com/ultrasound/products-by-family#02571109>, accessed Jan 30, 2018.
- [22] Q. Huang *et al.*, "Linear tracking for 3D medical ultrasound imaging," *IEEE Trans. Cybern.*, vol. 43, no. 6, pp. 1747–1754, 2013.
- [23] Q. Huang *et al.*, "Correspondence-3-D ultrasonic strain imaging based on a linear scanning system," *IEEE Trans. Ultrason., Ferroelectr., Freq. Control*, vol. 62, no. 2, pp. 392–400, 2015.
- [24] Z. Chen *et al.*, "Development of a wireless and near real-time 3Dultrasound strain imaging system," *IEEE Trans. Biomed. Circuits Syst.*, vol. 10, no. 2, pp. 394–403, 2016.
- [25] M. A. Janvier, *et al.*, "Performance evaluation of a medical robotic 3D-ultrasound imaging system," *Medical Image Analysis*, vol. 12, no. 3, pp. 275–290, 2008.
- [26] S. Merouche, *et al.*, "A robotic ultrasound scanner for automatic vessel tracking and three-dimensional reconstruction of B-mode images," *IEEE Trans. Ultrason., Ferroelectr. Freq.*, vol. 63, no. 1, pp. 35–46, 2016.
- [27] F. Conti, J. Park, and O. Khati, "Interface design and control strategies for a robot assisted ultrasonic examination system," *Experimental Robotics. Springer Tracts in Advanced Robotics*, vol. 79, pp. 97–113, 2014.
- [28] B. Meng *et al.*, "Robot-assisted mirror ultrasound scanning for deep venous thrombosis detection using RGB-D sensor," *Multimedia Tools & Applications*, vol. 75, no. 22, pp. 14247–14261, 2016.
- [29] Y. Wang, Z. Li, and C. Su, "RGB-D sensor-based visual SLAM for localization and navigation of indoor mobile robot," *International Conference on Advanced Robotics and Mechatronics*, pp. 82–87, 2016.
- [30] Q. Huang *et al.*, "Fully Automatic Three-Dimensional Ultrasound Imaging Based on Conventional B-Scan," *IEEE Trans. Biomed. Circuits Syst.*, to be published, DOI: 10.1109/TBCAS.2017.2782815.
- [31] R. W. Prager *et al.*, "Rapid calibration for 3D freehand ultrasound," *Ultrasound Med. Biol.*, vol. 24, no. 6, pp. 855–869, 1998.
- [32] J. J. Moré, "The Levenberg-Marquardt algorithm: Implementation and theory," *Lect Notes Math*, vol. 630, pp. 105–116, 1977.
- [33] A. Hartov *et al.*, "Error analysis for a free-hand three-dimensional ultrasound system for neuronavigation," *Neurosurgical Focus*, vol. 6, no. 3, 1999.
- [34] M. Alexa *et al.*, "Computing and rendering point set surfaces," *IEEE Trans. Vis. Comput. Graphics.*, vol. 9, no. 1, pp. 3–15, 2003.
- [35] Craig, John J, "Introduction to Robotics: Mechanics and Control," *Pearson Education*, Inc, 1986.
- [36] N. Koizumi *et al.*, "Construction methodology for a remote ultrasound diagnostic system," *IEEE Trans. Robot.*, vol. 25, no. 3, pp. 522–538, 2009.

- [37] K. Masuda *et al.*, "Development of support system to handle ultrasound probe by coordinated motion with medical robot," *Annu. Int. Conf. IEEE Engineering Medicine and Biology Society*, pp. 4519–4522, 2011.
- [38] M. W. Gilbertson and B. W. Anthony, "Force and Position Control System for Freehand Ultrasound," *IEEE Trans. Robot.*, vol. 31, no. 4, pp. 835–849, 2015.
- [39] Q. Huang *et al.*, "Bezier interpolation for 3D freehand ultrasound," *IEEE Trans. Human-Machine Syst.*, vol. 45, no. 3, pp. 385–392, 2015.